Computers and Fluids 188 (2019) 114–124

Contents lists available at ScienceDirect

Computers and Fluids

journal homepage: www.elsevier.com/locate/compfluid

Benchmark solutions

Residual-based variational multi-scale modeling for particle-laden gravity currents over flat and triangular wavy terrains

S. Xu, N. Liu, J. Yan*

Department of Civil and Environmental Engineering, University of Illinois at Urbana-Champaign, United States

ARTICLE INFO

Article history:
Received 20 November 2018
Revised 1 March 2019
Accepted 12 May 2019
Available online 17 May 2019

Keywords:
Particle-laden flows
RBVMS
Lock-exchange gravity currents

ABSTRACT

In this paper, a numerical formulation for simulating dilute particle-laden gravity currents at large Reynolds number (Re) is developed using a residual-based variational multi-scale formulation (RBVMS), in which the coupling between the velocity fine scales and density concentration equation residual is represented. The proposed formulation is utilized to simulate the lock-exchange particle-laden gravity currents at $Re = 10,000$. Firstly, we validated the proposed formulation by simulating the gravity currents over flat terrain. Flow statistics are thoroughly compared against high-resolution simulation results such as DNS or experimental results in the literature. It shows the RBVMS formulation presented here can reproduce quite accurate results with much lower mesh resolution. Then, the particle-laden gravity currents over triangular wavy terrains with changing wave heights are simulated. The effect of the wave height on the flow statistics is investigated.

Published by Elsevier Ltd.

1. Introduction

Many natural fluid dynamical processes involve complex particle-laden gravity currents. Examples of such flows in nature include thunderstorm fronts, volcano eruptions, oil spills in the ocean, snow avalanches, the release of contaminants in the environment, and flows generated by the collapse of a building [1,2]. Numerical study of particle-laden gravity currents is important for understanding the associated environmental and geophysical physics. To model the dilute particle-laden gravity currents, the Eulerian-Eulerian approach which consists of the Navier–Stokes (NS) equations of incompressible flows and an advection-diffusion transport equation is typically used [3–15]. The coupling between them is through the Boussinesq approximation introduced in the fluid momentum equation to represent the gravitational effect associated with small density variations. However, in many cases, these particle-laden gravity currents are extremely high-Reynolds number turbulent flows, in which the carrier fluid violently exchanges mass, momentum, and energy with a dispersed particle field, rendering accurate numerical simulations of particle-laden gravity currents quite challenging and expensive.

Recently, there were several successful numerical efforts for the simulations for particle-laden gravity currents [16–18]. Hartel et al. [11,12] utilized a spectral element method to investigate the 3D flow structure of the lock-exchange configuration. Necker et al. [19] presented 2D and 3D high-resolution simulations of particle-laden gravity currents also by spectral element method taking into account the sedimentation of the particles and the influence of particle settling on the flow dynamics. Elias et al. [20] developed a stabilized finite element formulation to simulate particle-laden gravity currents in both planar and cylindrical configurations. A variational multi-scale formulation for particle-laden gravity currents was developed by Guerra et al. [21]. Numerical methods using adaptive meshes for particle-laden gravity currents can be found in [22–25].

The paper aims to accurately simulate high Reynolds number particle-laden gravity currents in complex geometry configurations with relatively coarse mesh. Inspired by the research work [26–28], a residual-based variational multi-scale formulation (RBVMS), which represents the coupling between velocity field and density field in the fine-scale terms, is developed for particle-laden gravity currents in this paper. The original RBVMS was proposed in [29] for the simulation of incompressible turbulent flows. Since then, several research work in [27,30–40] have shown that RBVMS is able to produce accurate solutions on meshes with large-eddy simulation (LES)-level resolution that converge rapidly to the direct numerical simulation (DNS) results. The flexibility of RBVMS allows an easy extension to Arbitrary Lagrangian-Eulerian variational multiscale (ALE-VMS) framework [41–48], a moving domain formulation through the ALE technique, which is widely used in the applications of high-Reynolds CFD and fluid-structure interaction [39,40] with moving boundaries and interfaces, such as off-

* Corresponding author.
E-mail address: yjh@illinois.edu (J. Yan).

https://doi.org/10.1016/j.compfluid.2019.05.008
0045-7930/Published by Elsevier Ltd.

shore wind turbines and tidal turbines [49–51], compliant hydrofoils [52,53], patient-specific cardiovascular mechanics [54–57], vehicle engineering [58], gas turbines [59], long-span bridges [60], and bioprosthetic heart valves [61,62].

The proposed formulation is utilized to simulate the particle-laden gravity currents in the lock-exchange configuration. In this setup, two fluids with different densities are initially at rest and confined in a container, separated by a barrier. After the barrier is removed, due to gravity, the heavy fluid invades the light fluid resulting in a turbulent density current. Many fundamental physics, such as the turbulent structures of the currents, settling or resuspension, and their effects on the particle transport, can be represented in this setup by controlled laboratory tests or numerical simulations [63], with high fidelity experimental and computational data available in the literature [19,64]. In this paper, the particle-laden gravity currents in standard lock-exchange configuration with flat terrain is simulated first as the validation for the proposed formulation. Then, the particle-laden gravity currents over triangular wavy terrains with changing wave heights are simulated. The effect of the wave height on the flow statistics is investigated.

The governing equations of particle-laden gravity currents are presented in Section 2. The new RBVMS formulation is stated in Section 3. In Section 4.1, the particle-laden gravity currents in a lock-exchange configuration with flat terrain is simulated at Re = 10,000. Comparisons with direct numerical simulation (DNS) results and experimental results are presented in this section. In Section 4.2, the simulations of particle-laden gravity currents in a lock-exchange configuration with triangular wavy terrains are presented. The effect of wave height on flow physics is also discussed in this section. The conclusion is drawn in Section 5.

2. Governing equations of particle-laden gravity currents at the continuous level

In various situations of interest, the density difference in particle-laden gravity currents is less than 1%, making the Boussinesq approximation valid, in which the density is treated as constant in the momentum equations augmented with a body forcing term [3]. In this case, we can employ an Eulerian-Eulerian formulation, in which a continuum advection-diffusion equation is utilized to model the particle concentration field, instead of tracking individual particles in a Lagrangian fashion. In this paper, the particle diameter $\tilde{d}_p$ is assumed to be smaller than the Kolmogorov scale in turbulent flows, and the aerodynamic response time is assumed to be significantly smaller than the smallest time scale of the flow, making the particle Stokes number far less than 1.

Due to the small particle volume fraction of dilute gravity currents, we can assume that the fluid velocity is divergence free and the fluid-particle interaction is primarily through the exchange of momentum. The particles are transported by a velocity $\tilde{\boldsymbol{u}}_p$ that is obtained by superimposing the fluid velocity $\tilde{\boldsymbol{u}}$ and particle settling velocity $\tilde{u}_s\boldsymbol{e}_g$ in gravitational direction, and given as

$$\tilde{\boldsymbol{u}}_p = \tilde{\boldsymbol{u}} + \tilde{u}_s\boldsymbol{e}_g \tag{1}$$

where $\boldsymbol{e}_g$ is the unit vector in gravitational direction. Followed the Stokes' law, $\tilde{u}_s$ is obtained by balancing the gravitational force with the Stokes drag force $\tilde{\boldsymbol{F}} = 3\pi\tilde{\mu}\tilde{d}_p(\tilde{\boldsymbol{u}} - \tilde{\boldsymbol{u}}_p)$, and given as

$$\tilde{u}_s = \frac{\tilde{d}_p^2(\tilde{\rho}_p - \tilde{\rho}_1)\tilde{g}}{18\tilde{\mu}} \tag{2}$$

where $\tilde{\mu}$ is the dynamic viscosity of the carrier fluid, $\tilde{g}$ is the gravitational acceleration magnitude, $\tilde{\rho}_p$ is the density of the particle, and $\tilde{\rho}_1$ is the density of the carrier fluid. Note that the particle settling velocity is single-valued and the convective velocity for the particles is still divergence free.

With the above assumptions, the governing equations of dilute particle-laden gravity currents are stated as follows. The current motion is governed by the incompressible Navier–Stokes equations, which consist of a continuity equation and momentum equation augmented by the force exerted on the fluid by the particles. In dimensional form, these equations read

$$\tilde{\rho}_1\left(\frac{\partial\tilde{\boldsymbol{u}}}{\partial\tilde{t}} + \tilde{\boldsymbol{u}}\cdot\nabla\tilde{\boldsymbol{u}}\right) + \nabla\tilde{p} - \tilde{\mu}\Delta\tilde{\boldsymbol{u}} - \tilde{\boldsymbol{f}}_p = \boldsymbol{0} \tag{3}$$

$$\nabla\cdot\tilde{\boldsymbol{u}} = 0 \tag{4}$$

where, the additional forcing term in the momentum equation is given by $\tilde{\boldsymbol{f}}_p = \tilde{\rho}\tilde{g}\boldsymbol{e}_g$, $\tilde{\boldsymbol{u}}$ and $\tilde{p}$ are the current velocity and pressure, $\tilde{\rho}$ is the current density, $\tilde{\mu}$ is the dynamic viscosity of the current.

The evolution of the density field $\tilde{\rho}$ is governed by the following advection-diffusion equation

$$\frac{\partial\tilde{\rho}}{\partial\tilde{t}} + \tilde{\boldsymbol{u}}_p\cdot\nabla\tilde{\rho} - \tilde{\alpha}\Delta\tilde{\rho} = 0 \tag{5}$$

where $\tilde{\alpha}$ is the molecular diffusivity of the density field.

We can non-dimensionalize Eqs. (3), (4), and (5) by a reference length scale, such as the half-height $\tilde{H}/2$ of a lock-exchange flow domain, the carrier fluid density $\tilde{\rho}_1$, and the buoyancy velocity $\tilde{u}_b = \sqrt{\frac{\tilde{g}'\tilde{H}}{2}}$, where $\tilde{g}' = \tilde{g}\frac{\Delta\tilde{\rho}}{\tilde{\rho}_1}$ indicates the reduced gravitational acceleration vector. Provided the above scales, the non-dimensional time, fluid velocity, particle convective velocity, pressure and density can be given by

$$t = \frac{2\tilde{t}\tilde{u}_b}{\tilde{H}},\quad \boldsymbol{u} = \frac{\tilde{\boldsymbol{u}}}{\tilde{u}_b},\quad \boldsymbol{u}_p = \frac{\tilde{\boldsymbol{u}}_p}{\tilde{u}_b},\quad p = \frac{\tilde{p}}{\tilde{\rho}_1\tilde{u}_b^2},\quad \rho = \frac{\tilde{\rho} - \tilde{\rho}_l}{\Delta\tilde{\rho}} \tag{6}$$

In the above equations, $\Delta\tilde{\rho} = \tilde{\rho}_h - \tilde{\rho}_l$ denotes the difference between the densities of heavy ($\tilde{\rho}_h$) and light ($\tilde{\rho}_l$) fluids, respectively. After non-dimensionalization, we obtain

$$\frac{\partial\boldsymbol{u}}{\partial t} + \boldsymbol{u}\cdot\nabla\boldsymbol{u} + \nabla p - \frac{1}{Re}\Delta\boldsymbol{u} - \boldsymbol{f}_p = \boldsymbol{0} \tag{7}$$

$$\nabla\cdot\boldsymbol{u} = 0 \tag{8}$$

$$\frac{\partial\rho}{\partial t} + \boldsymbol{u}_p\cdot\nabla\rho - \frac{1}{ReS_c}\Delta\rho = 0 \tag{9}$$

where $\boldsymbol{f}_p = \rho\boldsymbol{e}_g$. The two dimensionless Reynolds number Re and Schmidt number S_c are defined as

$$Re = \frac{\tilde{\rho}_1\tilde{u}_b\tilde{H}}{2\tilde{\mu}} \tag{10}$$

$$S_c = \frac{\tilde{\mu}}{\tilde{\rho}_1\tilde{\alpha}} \tag{11}$$

The above equations, together with the appropriate initial and boundary conditions, constitute a complete mathematical model of particle-laden gravity currents at the continuous level.

3. Numerical formulation

3.1. Weak form

Let $\mathcal{V}$ denote the trial function space for the velocity, pressure, and density concentration unknowns $\{\boldsymbol{u}, p, \rho\}$, and let $\mathcal{W}$ denote the test function space for the momentum, continuity, density concentration equations $\{\mathbf{w}, q, \eta\}$. The weak form of the particle-laden gravity currents equations is stated as follows: find $\{\boldsymbol{u}, p, \rho\} \in \mathcal{V}$, such that $\forall\{\boldsymbol{w}, q, \eta\} \in \mathcal{W}$,

$$\boldsymbol{B}(\{\boldsymbol{w}, q, \eta\}, \{\boldsymbol{u}, p, \rho\}) = \boldsymbol{F}(\{\boldsymbol{w}, q, \eta\}) \tag{12}$$

where $\boldsymbol{B}$ and $\boldsymbol{F}$ are given as

$$\boldsymbol{B}(\{\boldsymbol{w}, q, \eta\}, \{\boldsymbol{u}, p, \rho\}) =$$

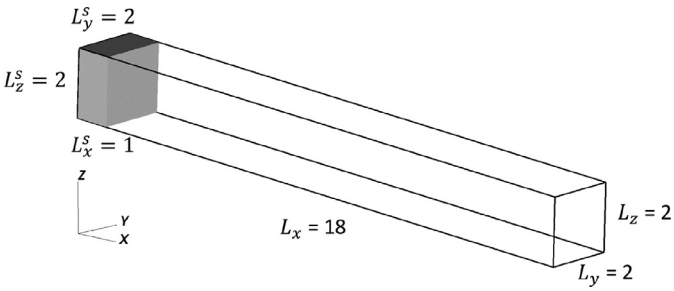

Fig. 1. Computational setup of lock-exchange particle-laden gravity currents over flat terrain.

$$\left(\boldsymbol{w}, \frac{\partial \boldsymbol{u}}{\partial t} + \boldsymbol{u}\cdot\nabla\boldsymbol{u}\right)_\Omega + \left(\nabla\boldsymbol{w}, -p\mathbf{I} + \frac{2}{Re}\nabla^S\boldsymbol{u}\right)_\Omega + \left(q, \nabla\cdot\boldsymbol{u}\right)_\Omega + \left(\boldsymbol{w}, \boldsymbol{f}_p\right)_\Omega + \left(\eta, \frac{\partial\rho}{\partial t} + \boldsymbol{u}_p\cdot\nabla\rho\right)_\Omega + \left(\nabla\eta, \frac{1}{ReS_c}\cdot\nabla\rho\right)_\Omega \tag{13}$$

$$\boldsymbol{F}(\{\boldsymbol{w}, q, \eta\}) = (\boldsymbol{w}, \boldsymbol{h})_{\Gamma_h} + (\eta, h)_{\Gamma_{h_p}} \tag{14}$$

where ∇^S is the symmetric gradient operator, $\boldsymbol{h}$ is the applied traction and h is the applied density flux.

3.2. RBVMS

The residual-based variational multi-scale formulation (RBVMS) is adopted to numerically solve the coupled Navier–Stokes and density concentration equations. In RBVMS, the trial function space and test function space are decomposed into two orthogonal parts, namely, $\mathcal{V} = \mathcal{V}^h \oplus \mathcal{V}'$ and $\mathcal{W} = \mathcal{W}^h \oplus \mathcal{W}'$, where the variables with superscript h denote the coarse-scale velocity, pressure, and density fields, which are resolved by the given problem mesh, and the variables with superscript $'$ denote the unresolved or fine-scale components, the effects of which on the solutions need to be modeled. With the above decomposition, the solution fields can be expressed as

$$\boldsymbol{u} = \boldsymbol{u}^h + \boldsymbol{u}' \tag{15}$$

$$p = p^h + p' \tag{16}$$

$$\rho = \rho^h + \rho' \tag{17}$$

Substituting the above decomposition into the weak form given by Eq. (12), and restricting the test functions to reside in the space of coarse-scales, gives the following semi-discrete RBVMS formulation: Find $\{\boldsymbol{u}^h, p^h, \rho^h\} \in \mathcal{V}^h$, such that $\forall\{\mathbf{w}^h, q^h, \eta^h\} \in \mathcal{W}^h$,

$$\boldsymbol{B}_{RBVMS}\left(\{\boldsymbol{w}^h, q^h, \eta^h\}, \{\boldsymbol{u}^h, p^h, \rho^h\}\right) = \boldsymbol{F}_{RBVMS}\left(\{\boldsymbol{w}^h, q^h, \eta^h\}\right) \tag{18}$$

where $\boldsymbol{B}_{RBVMS}$ and $\boldsymbol{F}_{RBVMS}$ are given as

$$\boldsymbol{B}_{RBVMS}\left(\{\boldsymbol{w}^h, q^h, \eta^h\}, \{\boldsymbol{u}^h, p^h, \rho^h\}\right) = \boldsymbol{B}\left(\{\boldsymbol{w}^h, q^h, \eta^h\}, \{\boldsymbol{u}^h, p^h, \rho^h\}\right) - \sum_{e=1}^{nel}\left(\boldsymbol{u}^h\cdot\nabla\boldsymbol{w}^h + \nabla q^h, \boldsymbol{u}'\right)_{\Omega^e} - \sum_{e=1}^{nel}\left(\nabla\cdot\boldsymbol{w}^h, p'\right)_{\Omega^e} + \sum_{e=1}^{nel}\left(\boldsymbol{w}^h, \boldsymbol{u}'\cdot\nabla\boldsymbol{u}^h\right)_{\Omega^e} - \sum_{e=1}^{nel}\left(\nabla\boldsymbol{w}^h, \boldsymbol{u}'\otimes\boldsymbol{u}'\right)_{\Omega^e} - \sum_{e=1}^{nel}\left(\boldsymbol{u}^h\cdot\nabla\eta^h, \rho'\right)_{\Omega^e} \tag{19}$$

$$\boldsymbol{F}_{RBVMS}\left(\{\boldsymbol{w}^h, q^h, \eta^h\}\right) = \boldsymbol{F}\left(\{\boldsymbol{w}^h, q^h, \eta^h\}\right) \tag{20}$$

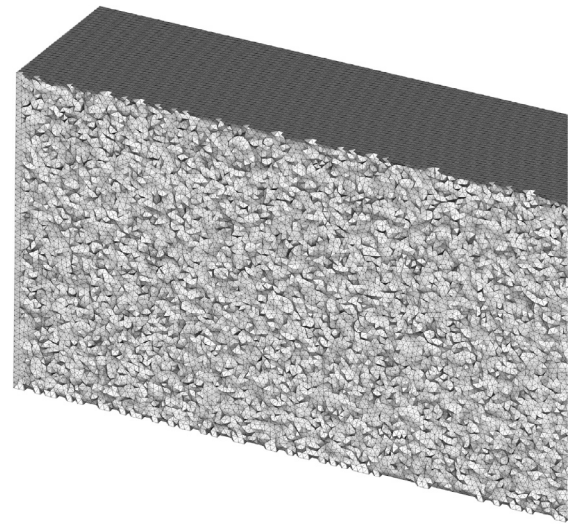

Fig. 2. Mesh around the inlet of the fine mesh.

In the above equation, the fine-scale velocity, pressure, and density concentration fields are modeled to be proportional to the residuals of the strong form momentum, continuity, and density concentration equations, given by

$$\begin{Bmatrix}\boldsymbol{u}' \\ \rho'\end{Bmatrix} = -\{\boldsymbol{\tau}\}\begin{Bmatrix}\boldsymbol{r}_m(\boldsymbol{u}^h, p^h, \rho^h) \\ r_\rho(\boldsymbol{u}^h, \rho^h)\end{Bmatrix} \tag{21}$$

$$p' = -\tau_c r_c(\boldsymbol{u}^h) \tag{22}$$

where $\boldsymbol{\tau}$ and τ_c are the fine-scale parameters, which will be given in the following section. $\boldsymbol{r}_m(\boldsymbol{u}^h, p^h, \rho^h)$, $r_c(\boldsymbol{u}^h)$ and $r_\rho(\boldsymbol{u}^h, \rho^h)$ are the residuals of momentum, continuity, and density concentration equations, given as

$$\boldsymbol{r}_m(\boldsymbol{u}^h, p^h, \rho^h) = \frac{\partial\boldsymbol{u}^h}{\partial t} + \boldsymbol{u}^h\cdot\nabla\boldsymbol{u}^h + \nabla p^h - \frac{1}{Re}\Delta\boldsymbol{u}^h - \rho^h\boldsymbol{e}_g \tag{23}$$

$$r_c(\boldsymbol{u}^h) = \nabla\cdot\boldsymbol{u}^h \tag{24}$$

$$r_\rho(\boldsymbol{u}^h, \rho^h) = \frac{\partial\rho^h}{\partial t} + \boldsymbol{u}_p^h\cdot\nabla\rho^h - \frac{1}{ReS_c}\Delta\rho^h \tag{25}$$

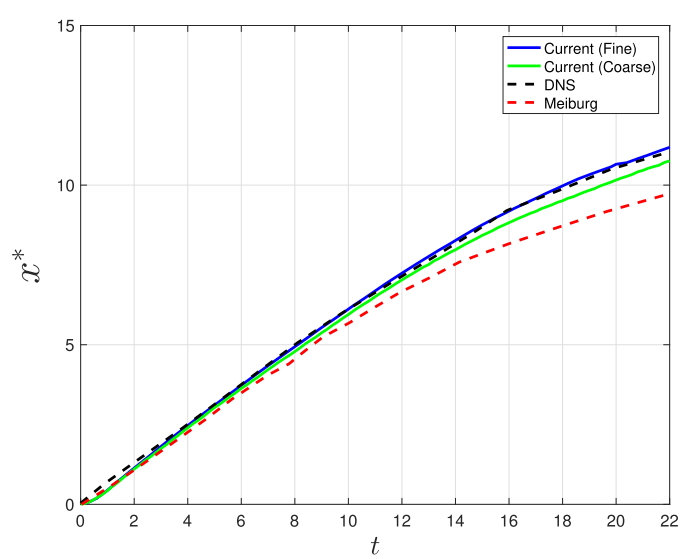

Fig. 3. Time history of the front location. The high-resolution simulation results in [19] and DNS results in [64] are also plotted for comparison.

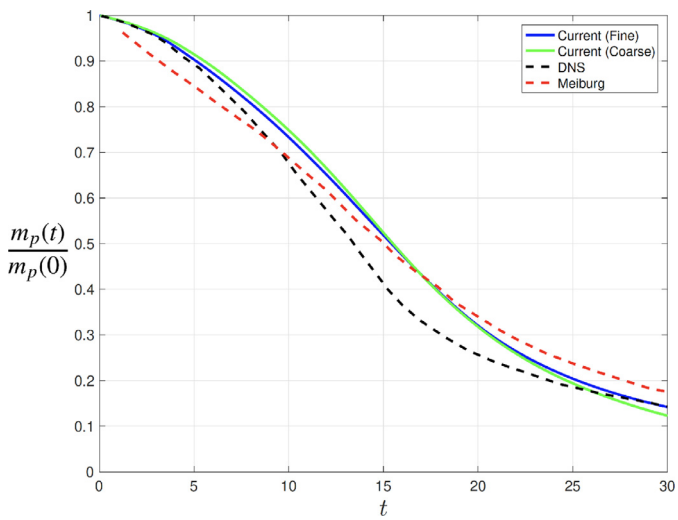

Fig. 4. Time history of the normalized suspended mass. The high-resolution simulation results in [19] and DNS results in [64] are also plotted for comparison.

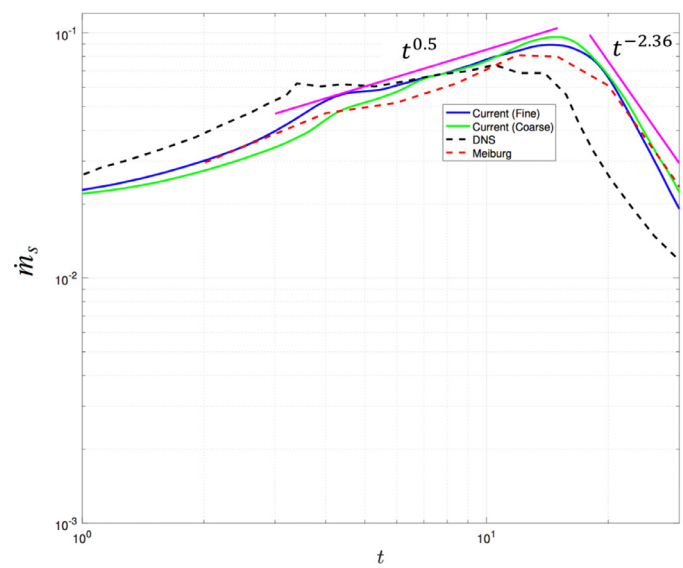

Fig. 5. Time history of sedimentation rate. The high-resolution simulation results in [19] and DNS results in [64] are also plotted for comparison.

3.3. Definition of the fine-scale parameters

In the traditional RBMVS approach, the fine-scale parameters $\boldsymbol{\tau}$ is a diagonal matrix. In the developments of stabilized methods for advective–diffusive systems and compressible flows presented in [65–67] and the recent development of RBVMS for stratified turbulent flows in [27], it shows that representing the coupling between advective–diffusive systems in the fine-scale parameters $\boldsymbol{\tau}$ enhances the performance of RBVMS simulations. In this paper, we adopt the same idea and design $\overline{\boldsymbol{\tau}}$ as

$$\left\{\overline{\boldsymbol{\tau}}\right\} = \boldsymbol{B}^{-\frac{1}{2}} \tag{26}$$

where $\boldsymbol{B}$ is given by

$$\boldsymbol{B} = \boldsymbol{A}_0^2 + \boldsymbol{A}_i G_{ij} \boldsymbol{A}_j + C_I \boldsymbol{K}^2 G_{ij} G_{ij} \tag{27}$$

where $\boldsymbol{A}_0$, $\boldsymbol{A}_i$ and $\boldsymbol{K}$ are defined as follows

$$\boldsymbol{A}_0 = \begin{Bmatrix} \frac{2}{\Delta t} & 0 & 0 & 0 \\ 0 & \frac{2}{\Delta t} & 0 & 0 \\ 0 & 0 & \frac{2}{\Delta t} & 1 \\ 0 & 0 & 0 & \frac{2}{\Delta t} \end{Bmatrix} \tag{28}$$

$$\boldsymbol{A}_i = \begin{Bmatrix} u_i \boldsymbol{I}_{3\times 3} & 0 \\ 0 & u_i + u_s \delta_{i3} \end{Bmatrix} \tag{29}$$

$$\boldsymbol{K} = \begin{Bmatrix} \frac{1}{Re} \boldsymbol{I}_{3\times 3} & 0 \\ 0 & \frac{1}{ReS_c} \end{Bmatrix} \tag{30}$$

where Δt is the time step, u_s is the non-dimensionalized settling velocity in the gravitational direction, $\boldsymbol{I}_{3\times 3}$ is the identity matrix,

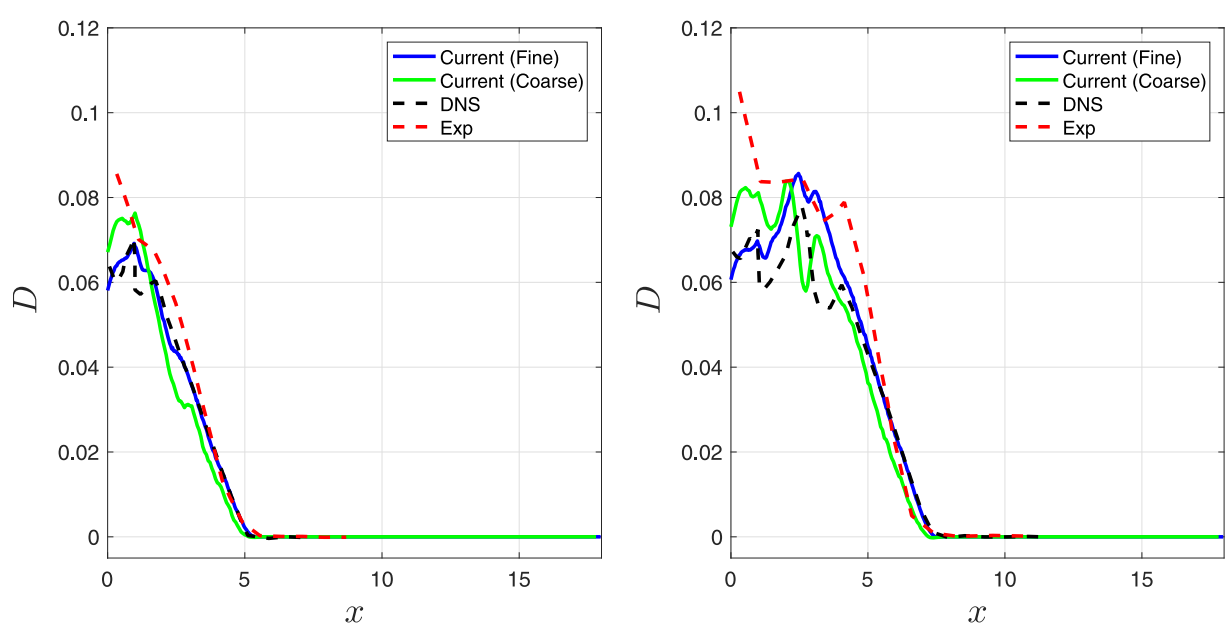

Fig. 6. Particle deposit $D(x, t)$ along stream-wise direction at $t = 7.3$ (left) and 11 (right). The experimental data in [75] and DNS results in [64] are also plotted for comparison.

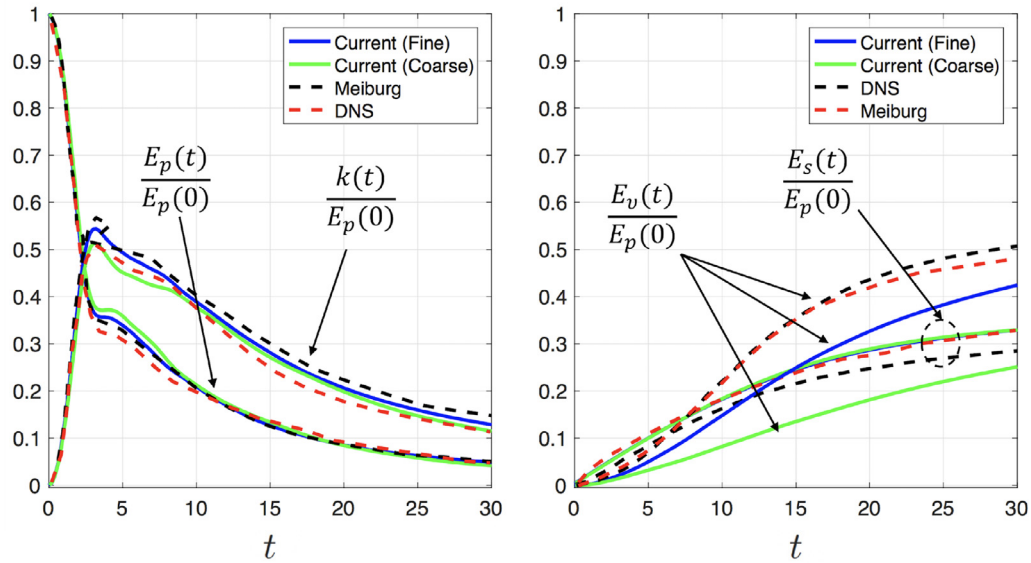

Fig. 7. Time history of kinetic energy $k(t)$, potential energy $E_p(t)$, the energy dissipations $E_v(t)$ and $E_s(t)$ normalized by the initial potential energy $E_p(0)$. The high-resolution simulation results in [19] and DNS results in [64] are also plotted for comparison.

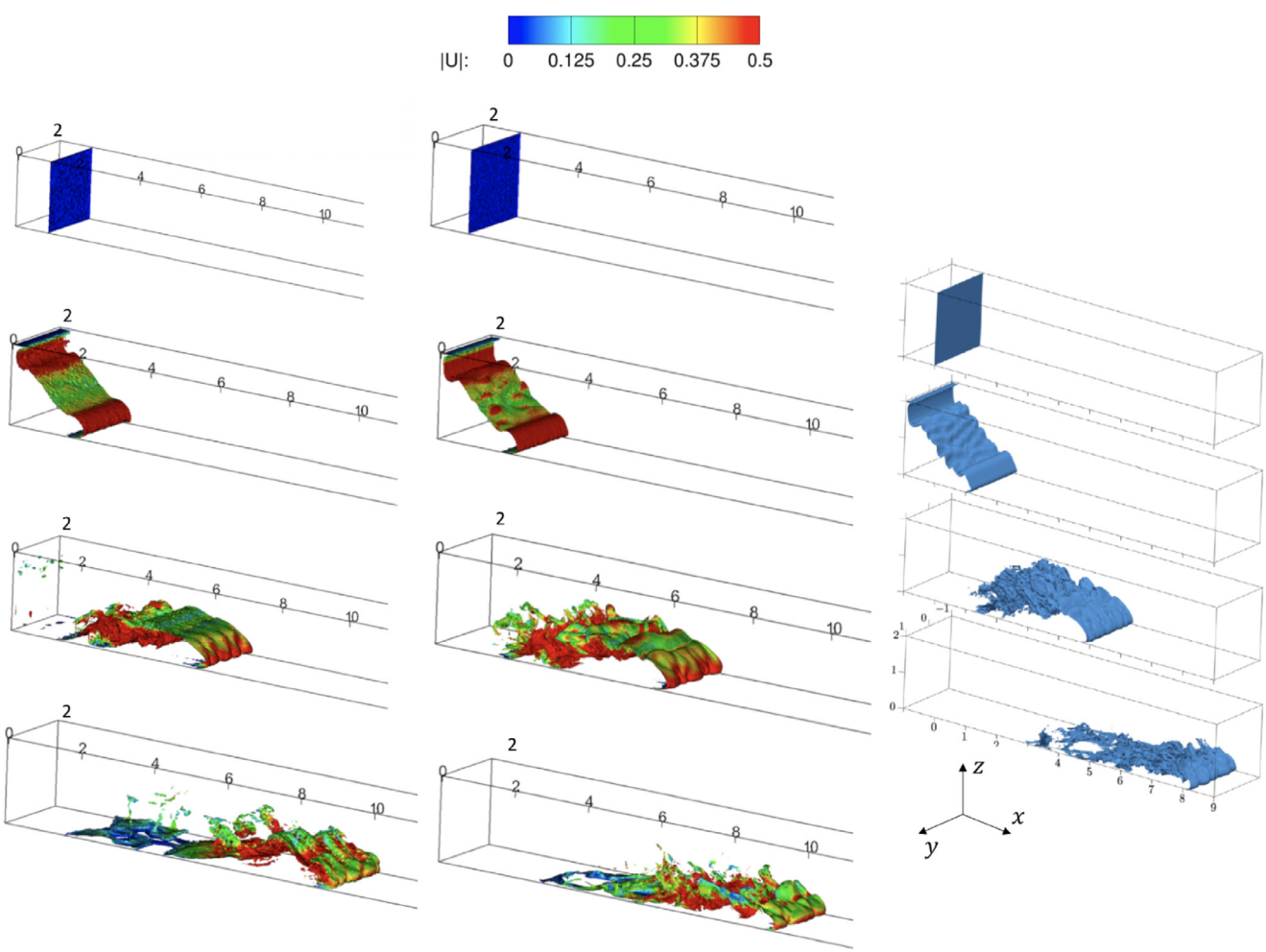

Fig. 8. Interface evolution of $\rho = 0.25$ ($t = 0$, 2, 8 and 14, from top to bottom; coarse mesh, fine mesh, and DNS results from Espath et al. [64], from left to right).

Table 1
Mesh statistics.

Meshes	Element length	Total number of nodes	Total number of elements
Coarse	0.066	447,392	2,537,166
Fine	0.033	3,485,389	20,150,859

and $\boldsymbol{G}$ is the element mesh metric tensor, given by $\boldsymbol{G} = \frac{\partial \boldsymbol{\xi}}{\partial \boldsymbol{x}} \frac{\partial \boldsymbol{\xi}}{\partial \boldsymbol{x}}^T$, where $\frac{\partial \boldsymbol{\xi}}{\partial \boldsymbol{x}}$ is Jacobian matrix of the mapping between the parametric element and its corresponding physical element.

Substitute $\boldsymbol{A}_0$, $\boldsymbol{A}_i$ and $\boldsymbol{K}$ into Eq. (27) and take the square-root-inverse analytically, the stabilization matrix $\boldsymbol{\tau}$ is computed as

$$\boldsymbol{\tau} = \begin{Bmatrix} \tau_m & 0 & 0 & 0 \\ 0 & \tau_m & 0 & 0 \\ 0 & 0 & \tau_m & \tau_{u\rho} \\ 0 & 0 & 0 & \tau_\rho \end{Bmatrix} \tag{31}$$

where τ_m and τ_c are

$$\tau_m = \left(\frac{4}{\Delta t^2} + \boldsymbol{u}^h \cdot \boldsymbol{G}\boldsymbol{u}^h + \frac{C_I}{Re^2} \boldsymbol{G} : \boldsymbol{G} \right)^{-1/2} \tag{32}$$

$$\tau_\rho = \left(\frac{4}{\Delta t^2} + (\boldsymbol{u}^h + u_s \boldsymbol{e}_g) \cdot \boldsymbol{G}(\boldsymbol{u}^h + u_s \boldsymbol{e}_g) + \frac{C_I}{Re^2 S_c^2} \boldsymbol{G} : \boldsymbol{G} \right)^{-1/2} \tag{33}$$

where C_I is a positive constant that is derived from an appropriate element-wise inverse estimate [68]. In the above stabilization matrix construction process, it turns out that τ_m and τ_ρ are the standard scalar-valued parameters employed in the standard RBVMS of incompressible flows and advection-diffusion equations [41–43,69–74]. The off-diagonal term $\tau_{u\rho}$, representing the coupling between velocity and density concentration fields, is given as

$$\tau_{u\rho} = -\frac{4}{\Delta t(\tau_m^{-1}\tau_\rho^{-2} + \tau_m^{-2}\tau_\rho^{-1})} \tag{34}$$

In this work, we assume the fine-scale parameter of pressure remains the usual definition, namely,

$$\tau_c = \frac{1}{tr(\boldsymbol{G})\tau_m} \tag{35}$$

4. Numerical examples

4.1. Lock-exchange particle-laden gravity currents over flat terrain

The problem of the lock-exchange gravity currents over flat terrain is solved by the proposed RBVMS formulation in this section. This problem is one of the most popular configurations for conducting laboratory experiments and high-resolution simulations on particle-laden gravity currents, which is a canonical example for validation purpose. The computational domain is a rectangular box with dimension $L_x \times L_y \times L_z$, where uniformly suspended particle sediments are initially enclosed in a small portion of the domain with dimension $L_x^s \times L_y^s \times L_z^s$ separated by a barrier with clear fluid. The computational setup is shown in Fig. 1. Due to gravity, a mutual inverse interaction between the "heavy" particle-mixture flow and "light" clear fluid will happen. Such a problem was investigated experimentally in [75] and computationally using DNS in [64] and high-resolution simulation in [19].

The simulation is performed using linear finite element discretizations using unstructured tetrahedral elements with a uniform element length. Two element lengths of 0.066 and 0.033 are employed, which are denoted by "coarse mesh" and "fine mesh" next. A snapshot of the fine mesh close to the inlet is shown in Fig. 2. The statistics of the mesh are listed in Table 1. The time step $\Delta t = 2 \times 10^{-3}$ is employed for coarse mesh and $\Delta t = 1 \times 10^{-3}$ is

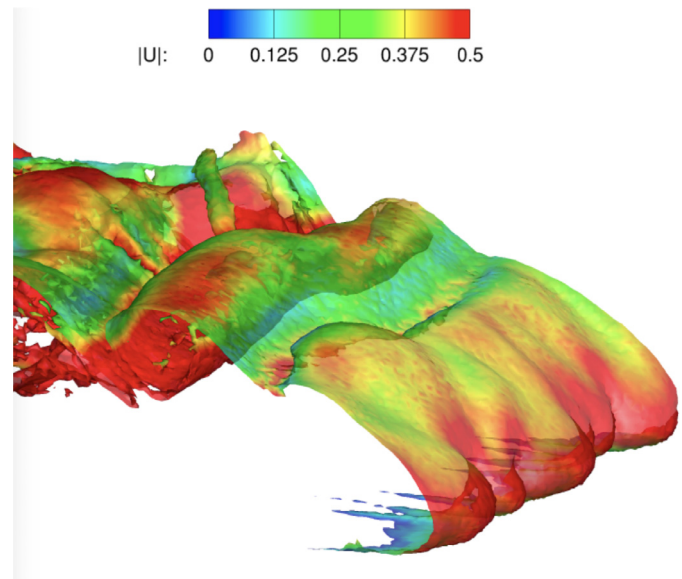

Fig. 9. Zoom-in of the current front in a concentration $\rho = 0.25$ at $t = 8$.

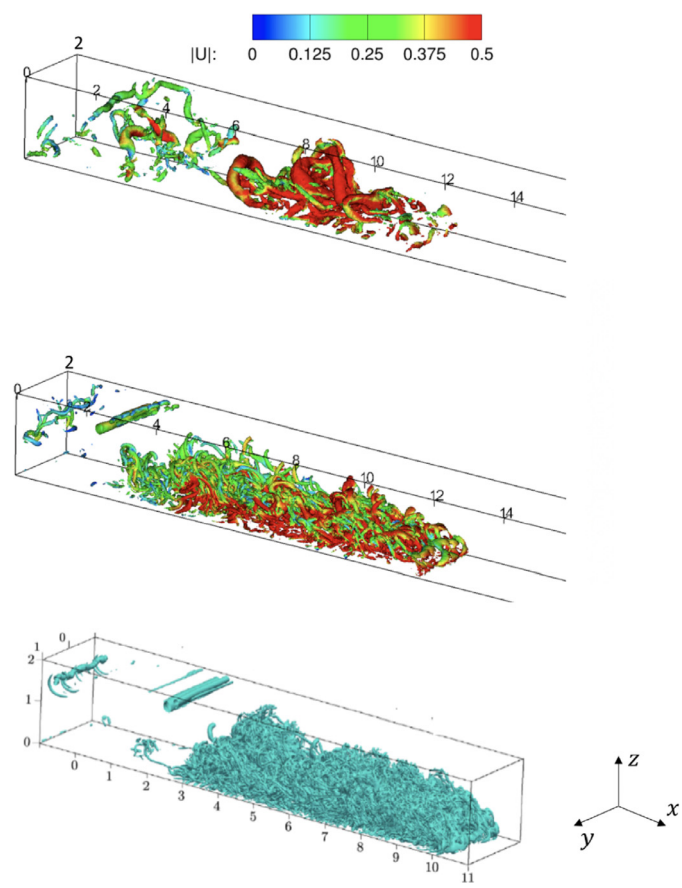

Fig. 10. Vorticity structure by isosurfaces of Q-criterion (for the isovalue $Q = 1$) at $t = 20$. (coarse mesh, fine mesh, and DNS results from Espath et al. [64], from top to bottom).

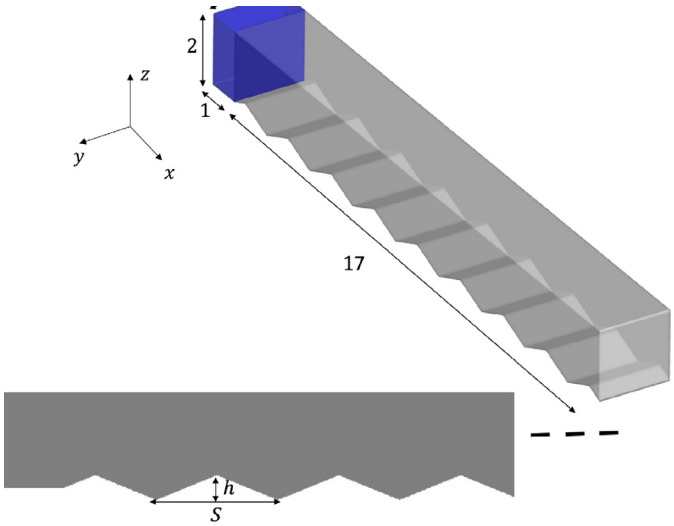

Fig. 11. Computational setup of particle-laden gravity currents over triangular wavy terrains.

employed for the fine mesh. We set settling velocity $u_s = 0.02$, the Schmidt number $S_c = 1$, and the Reynolds number $Re = 10,000$, which is the highest in the current literature.

The boundary conditions are given as follows. For fluid field, no penetration and free-slip boundary conditions are imposed for the velocity field in the stream-wise and span-wise directions while no-slip boundary conditions are used in the vertical direction. For the density field, at the bottom surface, no erosion and re-suspension are allowed, $u_s \boldsymbol{\nabla} \rho \cdot \boldsymbol{n} - \frac{\partial \rho}{\partial t} = 0$. No-flux boundary conditions are used for other surfaces.

The particle-laden gravity currents over flat terrain with the same parameters were also studied by DNS in [64] and high-resolution simulation in [19], where the element length is 8.45 times and 5.28 times finer, respectively, than the element length of the "coarse mesh" used in the present work. For more details of the grids utilized in these two computations, the readers are referred to the original papers in [64] and [19]. To validate the method, the results using the proposed formulation are thoroughly compared with these two computational results in [19,64], and experimental results in [75] for the flow statistics where such data is available.

Fig. 3 shows the time history of the front location $x^*(t)$ of the particle-laden gravity currents. Good agreement is achieved between the present results and the results from the DNS in [64] and the high-resolution simulation in [19]. The current front travels at a constant speed in the earlier stage but experiences a significant deceleration at later times due to particles settling. The settling of particles also causes a continued loss of suspended material in the domain. Fig. 4 shows the time history of the suspended mass normalized by the initial suspended mass $\frac{m_p(t)}{m_p(0)}$, where $m_p(t)$ is defined as

$$m_p(t) = \int_\Omega \rho d\Omega \tag{36}$$

Again, reasonable agreement with the two higher resolution simulations is achieved for both "coarse mesh" and "fine mesh". Rapid sedimentation process is observed in this plot. After $t = 21$, nearly 70% of all particles have settled out. Consequently, a sediment layer is formed at the bottom surface of the domain as time evolves. Fig. 5 shows the time history of the sedimentation rate $\dot{m}_s(t)$, which is defined as the time derivative of the total mass of sedimented particles per unit span.

$$\dot{m}_s(t) = \frac{1}{L_y} \int_0^{L_x} \int_0^{L_y} \rho_w(x, y, t) u_s dx dy \tag{37}$$

where ρ_w is the density concentration at the bottom wall. Good agreement with high-resolution simulation results is achieved for both "coarse mesh" and "fine mesh". Until t =14, the sedimentation rate steadily increases, which indicates that the suspension stretches out along the bottom and remains almost undiluted. In this stage, the increase is roughly proportional to $t^{0.5}$ in the logarithmic representation. However, after t =14, a dramatical decay of sedimentation rate with time is observed, which is roughly proportional to $t^{-2.36}$ in the logarithmic representation. This change occurs when about half of the particles have settled out, and it also coincides with the time when the front speed of the current starts to decrease (see Fig. 3).

Another important quantity of the sedimentation process is the stream-wise deposit of the sediment particles, which can be quantified as

$$D_t(x, t) = \frac{1}{L_z^s L_x^s} \int_0^t \rho_w(x, t) u_s d\tau \tag{38}$$

The profile of $D_t(x, t = 7.3)$ and $D_t(x, t = 11)$ are plotted in Fig. 6. For $Re =$ 10,000 and $u_s = 0.02$, experimental measurements are available in [75] and also plotted in Fig. 6 along with the DNS results. Good agreement with the experimental data and DNS results is seen for the both "coarse mesh" and "fine mesh". But clearly, the results based on fine mesh is closer to the DNS result.

In particle-laden gravity currents, the energy is converted from potential energy into fluid motion. The potential energy available is given by the elevation of the center of mass of the heavy fluid relative to the light fluid. If no potential energy is feed into the

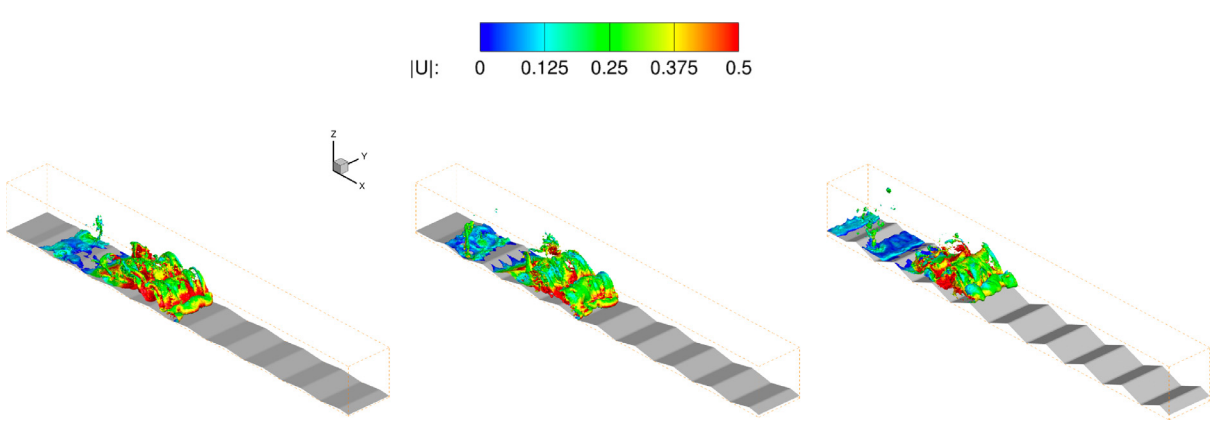

Fig. 12. Interface evolution of $\rho = 0.25$ of particle-laden gravity currents over triangular wavy terrains. ($h = 0.05$, 0.1 and 0.2, from left to right).

domain, the fluid motion will ultimately decay due to energy dissipations, which are caused by both convection gradients and the energy loss that particles experience due to progressive settling. For a time instant, the total potential energy $E_p(t)$, kinetic energy $k(t)$, and dissipated energy $E_v(t)$ and $E_s(t)$ are given as follows.

$$k(t) = \int_\Omega \frac{1}{2}\boldsymbol{u}\cdot\boldsymbol{u}d\Omega \tag{39}$$

$$E_p(t) = \int_\Omega \rho z d\Omega \tag{40}$$

$$E_v(t) = \int_0^t \left(\int_\Omega \frac{2}{Re}\boldsymbol{S}:\boldsymbol{S}d\Omega\right)d\tau \tag{41}$$

$$E_s(t) = \int_0^t \left(\int_\Omega u_s\rho d\Omega\right)d\tau \tag{42}$$

where $\boldsymbol{S} = \frac{1}{2}\left(\nabla\boldsymbol{u} + \nabla^T\boldsymbol{u}\right)$ is the symmetric part of the velocity gradient. The time history of the above four terms are plotted in Fig. 7. Good agreement is obtained for $k(t)$, $E_p(t)$ and $E_s(t)$. Please note the prediction of $E_s(t)$ is almost identical between the coarse and fine meshes. However, the dissipation due to the gradients of the (macroscopic) convective motion is underestimated, due to much lower resolution used in the present work.

Isosurfaces of a constant density concentration ($\rho = 0.25$) colored by velocity magnitude at five time instances are shown in Fig. 8. The DNS results from Espath et al. [64] are also shown for comparison. Both the coarse and fine meshes generate quite similar density profiles as the DNS does. At time t = 8, when the current is fully developed, the typical 3D lobe-and-cleft structure is observed in its front, as depicted in Fig. 9. It can be seen that as the time evolves, the current develops a high 3D turbulence with strong stream-wise vortices. This can be also supported by the complex vorticity structure visualized in Fig. 10, where the Q-criterion is adopted and defined as

$$Q = \frac{1}{2}(||\boldsymbol{\Omega}||^2 - ||\boldsymbol{S}||^2) \tag{43}$$

where $\boldsymbol{\Omega} = \frac{1}{2}\left(\nabla\boldsymbol{u} - \nabla^T\boldsymbol{u}\right)$ is the anti-symmetric part of the velocity gradient. In Fig. 10, we can see that the results from the coarse mesh lose some flow features of the vorticity structure due to lower mesh resolution, while the fine mesh produces quite similar vorticity structure like the DNS does.

4.2. Lock-exchange particle-laden gravity currents over triangular wavy terrain

In this section, the particle-laden gravity currents over triangular wavy terrain are simulated. The effect of the height of the triangular waves on the flow physics is investigated. Fig. 11 shows the computational domain, which consists with a rectangular section with the same dimensions as used in the previous section, where

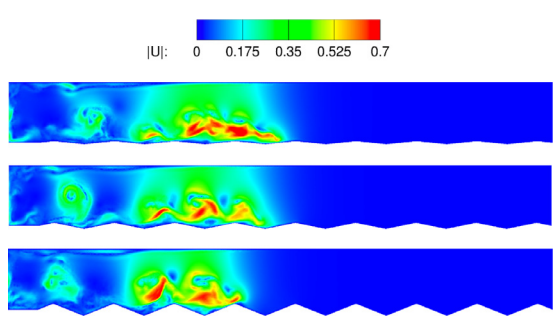

Fig. 13. Velocity magnitude of a plane cut ($y = 0$) of particle-laden gravity currents over triangular wavy terrains. (h = 0.05, 0.1 and 0.2, from top to bottom).

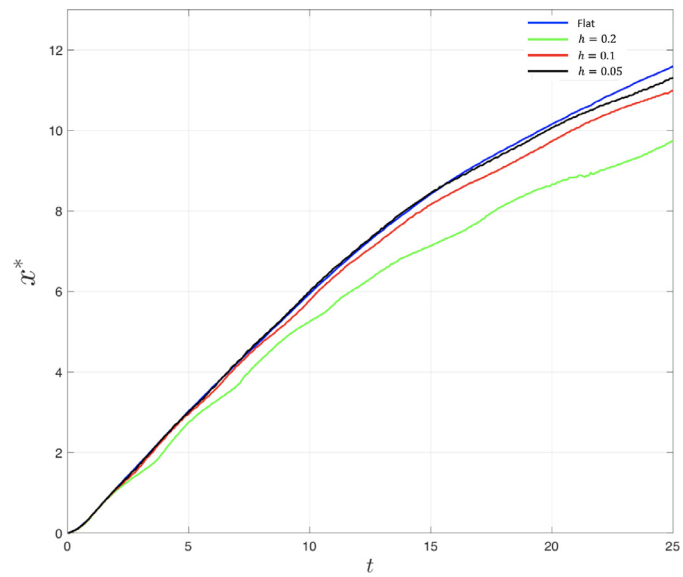

Fig. 14. Time history of the front location of particle-laden gravity currents over triangular wavy terrains.

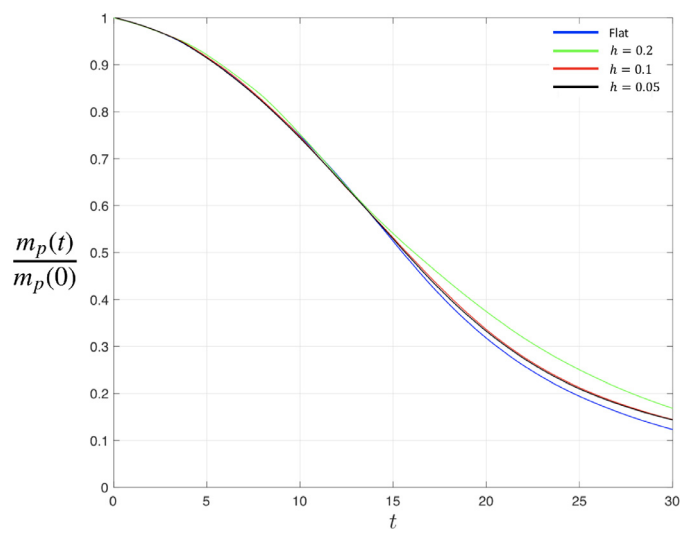

Fig. 15. Time history of the normalized suspended mass of particle-laden gravity currents over triangular wavy terrains.

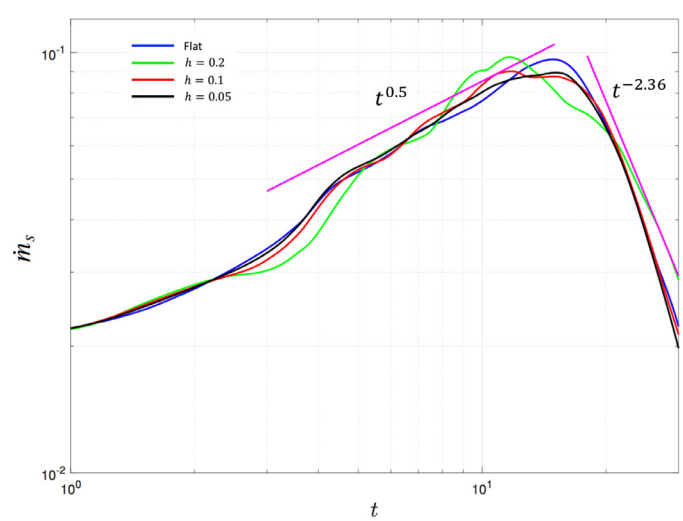

Fig. 16. Time history of the sedimentation rate of particle-laden gravity currents over triangular wavy terrains.

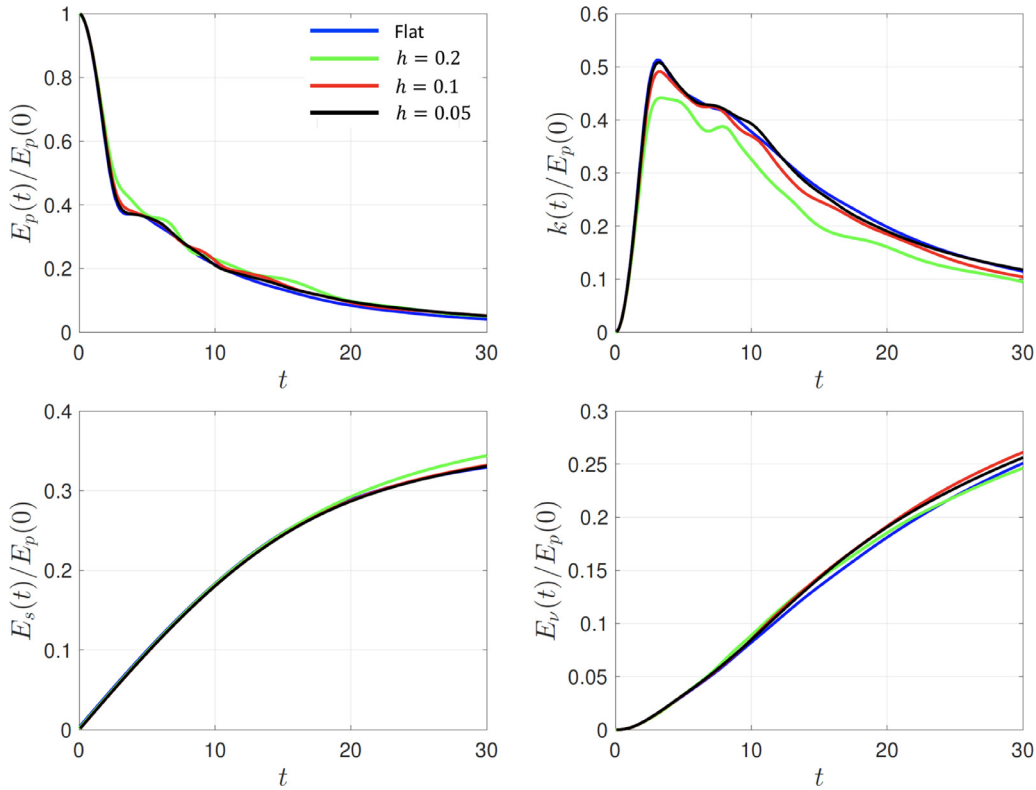

Fig. 17. Time history of the potential energy $E_p(t)$, kinetic energy $k(t)$, the energy dissipation $E_s(t)$, and $E_\nu(t)$ normalized by the initial potential energy $E_p(0)$.

uniformly suspended particle sediments are initially enclosed in, and a section with a triangular wavy bottom surface, with a length of 17. The length of the triangular waves is fixed to $S = 2$. Three different heights, $h = 0.05$, 0.1 and 0.2, are studied in this paper. Please note the case of $h = 0$ corresponds to the flat terrain case simulated in the previous section. In order to show the direct comparison with the flat terrain case, the same Reynolds number, Schmidt number, settling velocity, boundary conditions are employed. The element length and time step based on the coarse mesh in the previous section are used again.

The velocity magnitude profile of a plane cut ($y = 0$) is shown in Fig. 13. Jet-like flow is formed between the crests of the terrain. It can be seen that the current front travels slower as the wave heights increase. The isosurfaces of density concentration $\rho = 0.25$ colored by velocity magnitude of the three cases with triangular wavy terrain at $t = 14$ are visualized in Fig. 12. Fig. 14 shows the time history of the front location. As the wave height increases, the speed of the front head gradually becomes slower. When the front speed starts to decrease, arrives earlier as the wave height increases. The normalized suspended mass is shown in Fig. 15. Settling process becomes slower, as the wave height increases, which indicates that the triangular wavy bottom geometry not only decreases the front speed but also decreases the settling of particles. Fig. 16 shows the time history of sedimentation rate. When the wave height is not very high ($h = 0.05$ and 0.1), the sedimentation pattern is still quite similar to the flat terrain case, but for the case of $h = 0.2$, the sedimentation rate is noticeably changed. The power law of the increasing stage and delay stage of sedimentation rate no longer holds for this higher wave height case.

The time history of the normalized potential energy, kinetic energy, and energy dissipation are plotted in Fig. 17. For the cases of $h = 0.05$ and 0.1, the energy budget remains quite similar to the flat terrain case. But for $h = 0.2$, compared with other cases, we note the conversion of potential energy into kinetic energy becomes lower, while the energy dissipation due to particle settling becomes higher.

5. Conclusions

A numerical formulation for simulating particle-laden gravity currents is presented using the framework of RBVMS, in which the coupling between the fine-scale velocity and the residual of density concentration equation is represented. The simulation of lock-exchange particle-laden gravity currents over flat terrain is performed using the proposed formulation. The computed results are validated by high-resolution computational results and experimental results reported by other researchers. The proposed formulation is proved to be able to reproduce highly accurately results without using high mesh resolutions. Then the simulations of lock-exchange particle-laden gravity currents over triangular wavy terrains with different wave heights are performed. It was found the flow behavior is noticeably changed, as the wave height increases. Increasing the wave height will decrease the current front speed, slow down the particle settling, prohibit the conversion of potential energy into kinetic energy.

Acknowledgements

The support of this research from the University of Illinois at Urbana-Champaign is gratefully acknowledged.

References

[1] Simpson JE. Gravity currents: in the environment and the laboratory. Cambridge University Press; 1997.
[2] Benjamin TB. Gravity currents and related phenomena. J Fluid Mech 1968;31(2):209–48.
[3] Meiburg E, Radhakrishnan S, Nasr-Azadani M. Modeling gravity and turbidity currents: computational approaches and challenges. Appl Mech Rev 2015;67(4):040802.

[4] Meiburg E, Kneller B. Turbidity currents and their deposits. Ann Rev Fluid Mech 2010;42:135–56.
[5] Maxworthy T, Leilich J, Simpson J, Meiburg E. The propagation of a gravity current into a linearly stratified fluid. J Fluid Mech 2002;453:371–94.
[6] Huppert HE. Gravity currents: a personal perspective. J Fluid Mech 2006;554:299–322.
[7] Konopliv N, Smith SGL, McElwaine J, Meiburg E. Modelling gravity currents without an energy closure. J Fluid Mech 2016;789:806–29.
[8] Rottman JW, Simpson JE. Gravity currents produced by instantaneous releases of a heavy fluid in a rectangular channel. J Fluid Mech 1983;135:95–110.
[9] Gladstone C, Woods AW. On the application of box models to particle-driven gravity currents. J Fluid Mech 2000;416:187–95.
[10] Nasr-Azadani M, Meiburg E. Turbidity currents interacting with three-dimensional seafloor topography. J Fluid Mech 2014;745:409–43.
[11] Härtel C, Carlsson F, Thunblom M. Analysis and direct numerical simulation of the flow at a gravity-current head. Part 2. The lobe-and-cleft instability. J Fluid Mech 2000;418:213–29.
[12] Härtel C, Meiburg E, Necker F. Analysis and direct numerical simulation of the flow at a gravity-current head. Part 1. Flow topology and front speed for slip and no-slip boundaries. J Fluid Mech 2000;418:189–212.
[13] Necker F, Härtel C, Kleiser L, Meiburg E. Mixing and dissipation in particle–driven gravity currents. J Fluid Mech 2005;545:339–72.
[14] Gonzalez-Juez E, Meiburg E, Tokyay T, Constantinescu G. Gravity current flow past a circular cylinder: forces, wall shear stresses and implications for scour. J Fluid Mech 2010;649:69–102.
[15] Tokyay T, Constantinescu G, Meiburg E. Lock-exchange gravity currents with a high volume of release propagating over a periodic array of obstacles. J Fluid Mech 2011;672:570–605.
[16] Cantero MI, Lee J, Balachandar S, Garcia MH. On the front velocity of gravity currents. J Fluid Mech 2007;586:1–39.
[17] Marino B, Thomas L, Linden P. The front condition for gravity currents. J Fluid Mech 2005;536:49–78.
[18] Blanchette F, Strauss M, Meiburg E, Kneller B, Glinsky ME. High-resolution numerical simulations of resuspending gravity currents: conditions for self-sustainment. J Geophys Res 2005;110(C12).
[19] Necker F, Härtel C, Kleiser L, Meiburg E. High-resolution simulations of particle-driven gravity currents. Int J Multiph Flow 2002;28(2):279–300.
[20] Elias RN, Paraizo PL, Coutinho AL. Stabilized edge-based finite element computation of gravity currents in lock-exchange configurations. Int J Numer Methods Fluids 2008;57(9):1137–52.
[21] Guerra GM, Zio S, Camata JJ, Rochinha FA, Elias RN, Paraizo PL, et al. Numerical simulation of particle-laden flows by the residual-based variational multiscale method. Int J Numer Methods Fluids 2013;73(8):729–49.
[22] O'Callaghan J, Rickard G, Popinet S, Stevens C. Response of buoyant plumes to transient discharges investigated using an adaptive solver. J Geophys Res 2010;115(C11).
[23] Hiester H, Piggott M, Allison P. The impact of mesh adaptivity on the gravity current front speed in a two-dimensional lock-exchange. Ocean Modell 2011;38(1):1–21.
[24] Koltakov S, Fringer O. Moving grid method for numerical simulation of stratified flows. Int J Numer Methods Fluids 2013;71(12):1524–45.
[25] Rossa AL, Coutinho AL. Parallel adaptive simulation of gravity currents on the lock-exchange problem. Comput Fluids 2013;88:782–94.
[26] Bazilevs Y, Korobenko A, Yan J, Pal A, Gohari S, Sarkar S. Ale–vms formulation for stratified turbulent incompressible flows with applications. Math Models Methods Appl Sci 2015;25(12):2349–75.
[27] Yan J, Korobenko A, Tejada-Martínez A, Golshan R, Bazilevs Y. A new variational multiscale formulation for stratified incompressible turbulent flows. Comput Fluids 2016.
[28] Korobenko A, Yan J, Gohari S, Sarkar S, Bazilevs Y. Fsi simulation of two back--to-back wind turbines in atmospheric boundary layer flow. Comput Fluids 2017;158:167–75.
[29] Bazilevs Y, Calo VM, Cottrell JA, Hughes TJR, Reali A, Scovazzi G. Variational multiscale residual-based turbulence modeling for large eddy simulation of incompressible flows. Comput Methods Appl Mech Eng 2007;197:173–201.
[30] Takizawa K, Bazilevs Y, Tezduyar TE, Hsu M-C, Øiseth O, Mathisen KM, et al. Engineering analysis and design with ALE-VMS and Space–Time methods. Arch Comput Methods Eng 2014;21:481–508. doi:10.1007/s11831-014-9113-0.
[31] Takizawa K, Bazilevs Y, Tezduyar TE, Long CC, Marsden AL, Schjodt K. Space—Time and ALE-VMS methods for patient-specific cardiovascular fluid mechanics modeling. Math Models Methods Appl Sci 2014;24(12):2437–86.
[32] Bazilevs Y, Hsu M-C, Takizawa K, Tezduyar TE. ALE-VMS and ST-VMS methods for computer modeling of wind-turbine rotor aerodynamics and fluid–structure interaction. Math Models Methods ApplSci 2012;22(supp02):1230002.
[33] Bazilevs Y, Akkerman I. Large eddy simulation of turbulent Taylor–Couette flow using isogeometric analysis and the residual–based variational multiscale method. J Computat Phys 2010;229:3402–14.
[34] Bazilevs Y, Yan J, de Stadler M, Sarkar S. Computation of the flow over a sphere at Re= 3700: a comparison of uniform and turbulent inflow conditions. J Appl Mech 2014;81(12):121003.
[35] Golshan R, Tejada-Martínez AE, Juha M, Bazilevs Y. Large-eddy simulation with near-wall modeling using weakly enforced no-slip boundary conditions. Comput Fluids 2015;118:172–81.
[36] Tejada-MartÃnez AE, Akkerman I, Bazilevs Y. Large-eddy simulation of shallow water langmuir turbulence using isogeometric analysis and the residual-based variational multiscale method. J Appl Mech 2012;79(1):010909.
[37] Xu F, Schillinger D, Kamensky D, Varduhn V, Wang C, Hsu M-C. The tetrahedral finite cell method for fluids: immersogeometric analysis of turbulent flow around complex geometries. Comput Fluids 2015.
[38] van Opstal TM, Yan J, Coley C, Evans JA, Kvamsdal T, Bazilevs Y. Isogeometric divergence-conforming variational multiscale formulation of incompressible turbulent flows. Comput Methods Appl Mech Eng 2016.
[39] Bazilevs Y, Kamran K, Moutsanidis G, Benson D, Oñate E. A new formulation for air-blast fluid–structure interaction using an immersed approach. Part i: basic methodology and fem-based simulations. Comput Mech 2017:1–18.
[40] Bazilevs Y, Moutsanidis G, Bueno J, Kamran K, Kamensky D, Hillman M, et al. A new formulation for air-blast fluid–structure interaction using an immersed approach: part ii coupling of IGA and meshfree discretizations. Comput Mech 2017:1–16.
[41] Tezduyar TE. Stabilization parameters and element length scales in SUPG and PSPG formulations. In: Book of abstracts of an euro conference on numerical methods and computational mechanics, Miskolc, Hungary; 2002.
[42] Tezduyar TE. Computation of moving boundaries and interfaces with interface–tracking and interface-capturing techniques. In: Pre-conference proceedings of the sixth japan-us international symposium on flow simulation and modeling, Fukuoka, Japan; 2002.
[43] Tezduyar TE. Finite element methods for fluid dynamics with moving boundaries and interfaces. Encyclopedia of computational mechanics, vol 3: Fluids. John Wiley & Sons; 2004. chap. 17
[44] Tezduyar TE. Finite elements in fluids: stabilized formulations and moving boundaries and interfaces. Comput Fluids 2007;36:191–206. doi:10.1016/j.compfluid.2005.02.011.
[45] Tezduyar TE, Hughes TJR. Finite element formulations for convection dominated flows with particular emphasis on the compressible Euler equations. In: Proceedings of AIAA 21st aerospace sciences meeting. AIAA Paper 83–0125; Reno, Nevada; 1983.
[46] Bazilevs Y, Calo VM, Hughes TJR, Zhang Y. Isogeometric fluid–structure interaction: theory, algorithms, and computations. Comput Mech 2008;43:3–37.
[47] Bazilevs Y, Takizawa K, Tezduyar TE. Computational fluid-structure interaction: methods and applications. John Wiley & Sons; 2013.
[48] Tezduyar TE, Takizawa K, Bazilevs Y. Fluid–structure interaction and flows with moving boundaries and interfaces. In: Encyclopedia of computational mechanics; 2018. p. 1–53.
[49] Yan J, Korobenko A, Deng X, Bazilevs Y. Computational free-surface fluid–structure interaction with application to floating offshore wind turbines. Comput Fluids 2016.
[50] Yan J, Deng X, Korobenko A, Bazilevs Y. Free-surface flow modeling and simulation of horizontal-axis tidal-stream turbines. Comput Fluids 2016.
[51] Bazilevs Y, Korobenko A, Deng X, Yan J. Fluid–structure interaction modeling for fatigue-damage prediction in full-scale wind-turbine blades. J Appl Mech 2016;83(6):061010.
[52] Augier B, Yan J, Korobenko A, Czarnowski J, Ketterman G, Bazilevs Y. Experimental and numerical FSI study of compliant hydrofoils. Comput Mech 2015;55(6):1079–90.
[53] Yan J, Augier B, Korobenko A, Czarnowski J, Ketterman G, Bazilevs Y. FSI modeling of a propulsion system based on compliant hydrofoils in a tandem configuration. Comput Fluids 2016;141:201–11.
[54] Bazilevs Y, Calo VM, Zhang Y, Hughes TJR. Isogeometric fluid–structure interaction analysis with applications to arterial blood flow. Comput Mech 2006;38:310–22.
[55] Takizawa K, Bazilevs Y, Tezduyar TE. Space–time and ALE-VMS techniques for patient-specific cardiovascular fluid–structure interaction modeling. Arch Comput Methods Eng 2012;19:171–225. doi:10.1007/s11831-012-9071-3.
[56] Takizawa K, Bazilevs Y, Tezduyar TE, Long CC, Marsden AL, Schjodt K. ST and ALE-VMS methods for patient-specific cardiovascular fluid mechanics modeling. Math Models Methods Appl Sci 2014;24:2437–86.
[57] Takizawa K, Bazilevs Y, Tezduyar TE. Space–Time and ale-vms techniques for patient-specific cardiovascular fluid–structure interaction modeling. Arch Comput Methods Eng 2012;19(2):171–225.
[58] Takizawa K, Tezduyar TE, Kuraishi T. Multiscale Space–Time methods for thermo-fluid analysis of a ground vehicle and its tires. Math Models Methods Appl Sci 2015;25(12):2227–55.
[59] Xu F, Moutsanidis G, Kamensky D, Hsu M-C, Murugan M, Ghoshal A, et al. Compressible flows on moving domains: stabilized methods, weakly enforced essential boundary conditions, sliding interfaces, and application to gas-turbine modeling. Comput Fluids 2017;158:201–20.
[60] Helgedagsrud TA, Bazilevs Y, Korobenko A, Mathisen KM, Øiseth OA. Using ALE-VMS to compute aerodynamic derivatives of bridge sections. Comput Fluids 2018.
[61] Hsu M-C, Kamensky D, Bazilevs Y, Sacks MS, Hughes TJR. Fluid–structure interaction analysis of bioprosthetic heart valves: significance of arterial wall deformation. Comput Fluids 2014;54:1055–71. doi:10.1007/s00466-014-1059-4.
[62] Kamensky D, Hsu M-C, Schillinger D, Evans J, Aggarwal A, Bazilevs Y, et al. An immersogeometric variational framework for fluid–structure interaction: application to bioprosthetic heart valves. Comput Methods Appl Mech Eng 2015;284:1005–53.
[63] Constantinescu G. LES of lock-exchange compositional gravity currents: a brief review of some recent results. Environ Fluid Mech 2014;14(2):295–317.
[64] Espath L, Pinto L, Laizet S, Silvestrini J. Two-and three-dimensional direct numerical simulation of particle-laden gravity currents. Comput Geosci 2014;63:9–16.

[65] Shakib F, Hughes TJR, Johan Z. A multi-element group preconditionined GMRES algorithm for nonsymmetric systems arising in finite element analysis. Comput Methods Appl Mech Eng 1989;75:415–56.
[66] Hughes TJR, Mallet M. A new finite element formulation for computational fluid dynamics: III. The generalized streamline operator for multidimensional advective-diffusive systems. Comput Methods Appl Mech Eng 1986;58:305–28.
[67] Hughes TJR, Scovazzi G, Tezduyar TE. Stabilized methods for compressible flows. J Sci Comput 2010;43:343–68. doi:10.1007/s10915-008-9233-5.
[68] Harari I, Hughes TJ. What are c and h?: inequalities for the analysis and design of finite element methods. Comput Methods Appl Mech Engineering 1992;97(2):157–92.
[69] Brooks AN, Hughes TJR. Streamline upwind/Petrov-Galerkin formulations for convection dominated flows with particular emphasis on the incompressible Navier-Stokes equations. Comput Methods Appl Mech Eng 1982;32:199–259.
[70] Hsu M-C, Bazilevs Y, Calo VM, Tezduyar TE, Hughes TJR. Improving stability of stabilized and multiscale formulations in flow simulations at small time steps. Comput Methods Appl Mech Eng 2010;199:828–40. doi:10.1016/j.cma.2009.06.019.
[71] Takizawa K, Sathe S, Tezduyar TE. Incompressible flow computations with the multi-moment and SUPG/PSPG formulations. In: Proceedings of the third Asian-Pacific congress on computational mechanics (CD-ROM), Kyoto, Japan; 2007.
[72] Tezduyar T, Sathe S. Stabilization parameters in SUPG and PSPG formulations. J Comput Appl Mech 2003;4:71–88.
[73] Tezduyar TE, Liou J, Ganjoo DK, Behr M, Glowinski R. Unsteady incompressible flow computations with the finite element method. In: Chung TJ, editor. Finite elements in fluids, vol. 8. Hemisphere Publishing; 1992. p. 177–209.
[74] Tezduyar TE, Mittal S, Ray SE, Shih R. Incompressible flow computations with stabilized bilinear and linear equal-order-interpolation velocity-pressure elements. Comput Methods Appl Mech Eng 1992;95:221–42. doi:10.1016/0045-7825(92)90141-6.
[75] De Rooij F, Dalziel S. Time- and space-resolved measurements of deposition under turbidity currents. Particulate Gravity Currents 2001:207–15.